

Magnetic Quantum Dots: Synthesis, Spectroscopy, and Magnetism of Co²⁺- and Ni²⁺-Doped ZnO Nanocrystals

Dana A. Schwartz, Nick S. Norberg, Quyen P. Nguyen, Jason M. Parker, and Daniel R. Gamelin*

Contribution from the Department of Chemistry, Box 351700, University of Washington, Seattle, Washington 98195-1700

Received June 20, 2003; E-mail: Gamelin@chem.washington.edu.

Abstract: We report a method for the preparation of colloidal ZnO-diluted magnetic semiconductor quantum dots (DMS-QDs) by alkaline-activated hydrolysis and condensation of zinc acetate solutions in dimethyl sulfoxide (DMSO). Mechanistic studies reveal that Co²⁺ and Ni²⁺ dopants inhibit nucleation and growth of ZnO nanocrystals. In particular, dopants are quantitatively excluded from the critical nuclei but are incorporated nearly isotropically during subsequent growth of the nanocrystals. The smaller nanocrystal diameters that result upon doping are explained by the Gibbs–Thompson relationship between lattice strain and crystal solubility. We describe methods for cleaning the nanocrystal surfaces of exposed dopants and for redispersion of the final DMS-QDs. Homogeneous substitutional doping is verified by high-resolution low-temperature electronic absorption and magnetic circular dichroism (MCD) spectroscopies. A “giant Zeeman effect” is observed in the band gap transition of Co²⁺:ZnO DMS-QDs. MCD and Zeeman spectroscopies are used to quantify the magnitude of the p–d exchange interaction ($N_0\beta$) that gives rise to this effect. $N_0\beta$ values of -2.3 ± 0.3 eV ($-18\,500$ cm⁻¹) for Co²⁺:ZnO and -4.5 ± 0.6 eV ($-36\,300$ cm⁻¹) for Ni²⁺:ZnO have been determined. Ligand-to-metal charge-transfer transitions are observed in the MCD spectra of both Co²⁺:ZnO and Ni²⁺:ZnO DMS-QDs and are analyzed in the context of an optical electronegativity model. The importance of these charge-transfer states in determining $N_0\beta$ is discussed. Ferromagnetism with $T_C > 350$ K is observed in aggregated nanocrystals of Co²⁺:ZnO that unambiguously demonstrates the existence of intrinsic high- T_C ferromagnetism in this class of DMSs.

I. Introduction

Diluted magnetic semiconductors (DMSs)¹ are currently attracting intense interest in the emerging field of spin-based electronics, or “spintronics.”^{2,3} The broad objective of this field is to control electron spins, in addition to charges, in order to transmit information and provide new functionality to semiconductor devices. Operational spin-dependent light-emitting diodes (spin LEDs) have been demonstrated that use II–VI and III–V DMSs as the key spin-polarization materials.³ The ultimate utility of these prototype devices has been limited, however, by the low ferromagnetic ordering temperatures of the DMSs used ($T_C \leq \sim 110$ K). The development of high- T_C ferromagnetic DMSs thus remains a central challenge confronting this field. Using computational methods, researchers have recently proposed that TM²⁺-doped ZnO DMSs should be

favorable candidates for room-temperature ferromagnetism.^{4,5} Experimental tests of these predictions have yielded inconsistent results. Room-temperature ferromagnetism has been reported for some Co²⁺-, Fe²⁺-, and V²⁺-doped ZnO thin films synthesized by vacuum deposition methods such as pulsed laser deposition,^{6–8} but several studies also report the absence of ferromagnetism in similar films.^{6,9,10} This class of materials appears to be extremely sensitive to the conditions of sample preparation and postsynthetic treatment, and the ultimate source of the observed ferromagnetism remains controversial. Some authors have suggested that the strong sensitivity to preparative conditions results from the relatively uncontrolled formation of lattice defects,^{6,7} which are proposed to generate carriers that mediate ferromagnetic ordering.^{4,5,11} Other authors, however,

- (1) Furdyna, J. K.; Kossut, J. In *Semiconductors and Semimetals*; Willardson, R. K., Beer, A. C., Eds.; Academic: New York, 1988; Vol. 25.
- (2) (a) Ohno, H.; Chiba, D.; Matsukura, F.; Omiya, T.; Abe, E.; Dietl, T.; Ohno, Y.; Ohtani, K. *Nature* **2000**, *408*, 944–946. (b) Wolf, S. A.; Awschalom, D. D.; Buhrman, R. A.; Daughton, J. M.; von Molnar, S.; Roukes, M. L.; Chtchelkanova, A. Y.; Treger, D. M. *Science* **2001**, *294*, 1488–1495. (c) Awschalom, D. D.; Flatté, M. E.; Samarth, N. *Sci. Am.* **2002**, *286*, 66–73.
- (3) (a) Ohno, Y.; Young, D. K.; Beschoten, B.; Matsukura, F.; Ohno, H.; Awschalom, D. D. *Nature* **1999**, *402*, 790–792. (b) Flederling, R.; Keim, M.; Reuscher, G.; Ossau, W.; Schmidt, G.; Waag, A.; Molenkamp, L. W. *Nature* **1999**, *402*, 787–790. (c) Jonker, B. T.; Park, Y. D.; Bennett, B. R.; Cheong, H. D.; Kioseoglou, G.; Petrou, A. *Phys. Rev. B: Condens. Matter* **2000**, *62*, 8180–8183.

- (4) (a) Sato, K.; Katayama-Yoshida, H. *Physica B* **2001**, *308–310*, 904–907. (b) Sato, K.; Katayama-Yoshida, H. *Physica E* **2001**, *10*, 251–255.
- (5) Dietl, T.; Ohno, H.; Matsukura, F.; Cibert, J.; Ferrand, D. *Science* **2000**, *287*, 1019–1022.
- (6) Ueda, K.; Tabata, H.; Kawai, T. *Appl. Phys. Lett.* **2001**, *79*, 988–990.
- (7) (a) Cho, Y. M.; Choo, W. K.; Kim, H.; Kim, D.; Ihm, Y. *Appl. Phys. Lett.* **2002**, *80*, 3358–3360. (b) Saeki, H.; Tabata, H.; Kawai, T. *Solid State Commun.* **2001**, *120*, 439–443.
- (8) Norton, D. P.; Pearton, S. J.; Hebard, A. F.; Theodoropoulou, N.; Boatner, L. A.; Wilson, R. G. *Appl. Phys. Lett.* **2003**, *82*, 239–241.
- (9) Ando, K.; Saito, H.; Jin, Z.; Fukumura, T.; Kawasaki, M.; Matsumoto, Y.; Koinuma, H. *Appl. Phys. Lett.* **2001**, *78*, 2700–2702.
- (10) Jin, Z.-W.; Fukumura, T.; Hasegawa, K.; Yoo, Y.-Z.; Ando, K.; Sekiguchi, T.; Ahmet, P.; Chikyow, T.; Hasegawa, T.; Koinuma, H.; Kawasaki, M. *J. Cryst. Growth* **2002**, *237–239*, 548–552.

claim that in at least some instances phase-segregated metal nanocrystals or other precipitates are responsible for the observed ferromagnetism,¹² thereby questioning the existence of intrinsic high- T_C ferromagnetism in these DMSs. Understanding and controlling ferromagnetic ordering in DMSs thus remains a significant challenge.

The difficulties in controlling the chemical properties of DMSs synthesized by vacuum deposition methods have motivated us to investigate direct chemical methods for the synthesis of DMSs. Our hypothesis is that direct synthetic methods may allow better control over chemical composition and dopant speciation than the vacuum deposition methods and may therefore provide a better experimental basis for understanding and ultimately controlling the magnetic properties of this class of materials. Furthermore, a direct chemical approach may allow DMSs to be prepared in unprecedented forms, such as the colloidal ZnO DMS quantum dots (DMS-QDs) reported here and communicated previously.¹³ Nanoscale DMSs, including quantum dots, quantum wells, and quantum wires, are envisioned as pivotal architectural elements in several spintronics devices.^{2,3} Spin effects in nanoscale semiconductors are still largely unexplored, however, and many essential advances in this field would be facilitated by the development of facile methods for the preparation of high-quality DMS nanocrystals. Finally, solution syntheses offer attractive advantages for scaled up production and processing relative to alternative gas-phase methods.

A major practical challenge in the synthesis of DMS nanostructures is that of dopant incorporation. Previous experimental studies have demonstrated the tendency for dopant ions to be excluded during nanocrystal synthesis.^{14,15} Surface-bound dopants may have different geometries, ligation, and exchange coupling interactions with the semiconductor band electrons than substitutionally incorporated dopants have. The target physical properties of the DMS may therefore be compromised if care is not taken to ensure substitutional doping. A closely related challenge, however, is that of determining experimentally the speciation and spatial distribution of dopants in crystals of nanometer dimensions.

We have recently communicated the synthesis of colloidal TM^{2+} -doped ZnO DMS-QDs, in which ethanol was used as the solvent.¹³ In this paper, we report a new synthetic procedure that uses DMSO as the solvent and that excels in allowing gram quantities of high-quality DMS-QDs to be prepared rapidly and with high reproducibility. Ligand-field electronic absorption spectroscopy has been applied to monitor dopant incorporation into nanocrystals during synthesis. We have found that dopants are quantitatively excluded from the initial nucleation event but are incorporated into the ZnO nanocrystals nearly isotropically during growth from solution and that dopants inhibit both the nucleation and growth of ZnO. We further demonstrate an effective method for removing dopants from the surfaces of the as-synthesized nanocrystals. This new procedure ultimately

yields highly dispersible colloidal ZnO DMS-QDs of relatively uniform size and shape, and most importantly, of uniform dopant speciation. In the absence of direct experimental determination, it has been commonly assumed that substitutional dopants are isotropically distributed throughout the semiconductor nanocrystals. To our knowledge, there have been no prior experimental studies of dopant spatial distributions *within* DMS nanocrystals.

The purpose of synthesizing high-quality DMS-QDs is to study their physical properties. Low-temperature electronic absorption, magnetic circular dichroism (MCD), Zeeman, and magnetic susceptibility techniques have been applied to study the electronic structural properties of these DMS-QDs. We have observed giant excitonic Zeeman splittings and, through observation and assignment of a sub-bandgap charge-transfer transition, we have related the magnitudes of these splittings to the covalencies of the dopant-host bonds. Finally, we have observed that reaction-limited aggregation of paramagnetic Co^{2+} :ZnO DMS-QDs at room temperature gives rise to robust ferromagnetic ordering with $T_C > 350$ K, and we discuss the reasons behind this transformation. This result, in which low-temperature solution chemical methods have been used to induce long-range magnetic ordering, unambiguously demonstrates the existence of intrinsic high- T_C ferromagnetism in Co^{2+} :ZnO DMSs.

II. Experimental Section

A. Sample Preparation. Colloidal nanocrystalline ZnO was synthesized at room temperature by the addition of an ethanolic solution of tetramethylammonium hydroxide ($\text{N}(\text{Me})_4\text{OH}\cdot 5\text{H}_2\text{O}$) to $\text{Zn}(\text{OAc})_2\cdot 2\text{H}_2\text{O}$ dissolved in DMSO. In a typical preparation, 30 mL of 0.552 M $\text{N}(\text{Me})_4\text{OH}$ in EtOH (1.8 equiv of OH^-) was added dropwise at approximately 2 mL/min to a 90-mL solution of 0.101 M $\text{Zn}(\text{OAc})_2$ in DMSO under constant stirring. Transition-metal doping was achieved by addition of $\text{Co}(\text{OAc})_2\cdot 4\text{H}_2\text{O}$ or $\text{Ni}(\text{ClO}_4)_2\cdot 6\text{H}_2\text{O}$ to the $\text{Zn}(\text{OAc})_2\cdot 2\text{H}_2\text{O}$ precursor solution. In our doping experiments, the concentration of zinc ions was reduced to keep the total initial concentration of metal ions constant. Nanocrystals prepared in this way may be precipitated from DMSO by addition of ethyl acetate or heptane, washed with ethyl acetate, and resuspended in DMSO or ethanol. Addition of ~ 10 mg of $\text{Zn}(\text{OAc})_2$ to a cloudy suspension of nanocrystalline ZnO will restore the optical clarity of the suspension. Aggregates of Co^{2+} :ZnO nanocrystals were prepared by simply allowing the solvent to evaporate from a concentrated ethanol suspension of nanocrystals in air on a benchtop at room temperature.

For treatment with trioctylphosphine oxide (TOPO),¹⁶ washed nanocrystals were precipitated from DMSO by addition of dodecylamine and washed with ethanol to remove DMSO. Care was taken to remove all excess Zn^{2+} precursor from the DMSO solution prior to addition of the amine, since the amine causes rapid growth of the nanocrystals at the expense of size uniformity. The dodecylamine-capped nanocrystals were then resuspended in toluene and precipitated with ethanol twice. The resulting powder was heated in TOPO at 180 °C for at least 30 min. The TOPO-treated nanocrystals were cooled to below 80 °C, precipitated, and washed with ethanol. The resulting powders may be resuspended (with addition of 1 mg of additional TOPO) in a variety of nonpolar solvents to form stable, high-optical-quality colloidal solutions. Concentrations of ZnO QDs in toluene in excess of 0.4 g/mL have been achieved and appear to remain stable indefinitely with no indication of growth, aggregation, dopant mobility, or precipitation.

- (11) (a) Dietl, T. *Semicond. Sci. Technol.* **2002**, *17*, 377–392. (b) Sawicki, M.; van Khoi, L.; Matsukura, F.; Dietl, T.; Fukumura, T.; Jin, Z.; Koinuma, H.; Kawasaki, M. *J. Supercond.* **2003**, *16*, 147–150.
- (12) Ando, K. *cond-mat/0208010*.
- (13) Radovanovic, P. V.; Norberg, N. S.; McNally, K. E.; Gamelin, D. R. *J. Am. Chem. Soc.* **2002**, *124*, 15192–15193.
- (14) Radovanovic, P. V.; Gamelin, D. R. *J. Am. Chem. Soc.* **2001**, *123*, 12207–12214.
- (15) Mikulec, F. V.; Kuno, M.; Bennati, M.; Hall, D. A.; Griffin, R. G.; Bawendi, M. G. *J. Am. Chem. Soc.* **2000**, *122*, 2532–2540.

- (16) We used technical grade TOPO (Aldrich) which contains phosphonic acids that have been shown to be the primary species responsible for ligation of CdSe QDs. An analogous role for the phosphonic acids in this ZnO preparation is likely. See Peng, Z. A.; Peng, X. *J. Am. Chem. Soc.* **2002**, *124*, 3343–3353.

B. Physical Measurements. X-ray powder diffraction data were collected on a Philips PW 1830 X-ray diffractometer. High-resolution electron microscopy (HREM) and electron diffraction images were collected at the Pacific Northwest National Laboratories on a JEOL 2010 transmission electron microscope (200 kV) with a high-brightness LaB₆ filament as an electron source. Dopant concentrations were determined by inductively coupled plasma atomic emission spectrometry (ICP-AES, Jarrel Ash model 955). SEM data were collected on a Serion XL-30 field emission electron microscope.

Electronic absorption spectra were collected using a Cary 5E (Varian) spectrophotometer. At room temperature, colloidal samples were handled in 1.0-cm path-length quartz cuvettes. For routine measurements, average nanocrystal diameters were estimated from the empirical tight-binding model relationships between band gap absorption energies and crystallite diameters,^{17,18} which agreed well with the Scherrer analysis of XRD peak widths for the same samples. For select cases, diameters were additionally verified by TEM measurements.

Electronic absorption spectra (7 K) were collected on TOPO-treated nanocrystals spin-coated as films on quartz disks or prepared as frozen solutions (glasses) and cooled by helium vapor using a Janis STVP-100 continuous-flow optical cryostat mounted in the Cary 5E absorption spectrophotometer. MCD spectra were collected on the same samples using a UV/VIS/NIR magnetic circular dichroism spectrophotometer constructed from an Aviv 40DS spectropolarimeter with a sample compartment modified to house a high-field superconducting magneto-optical cryostat. The CryoIndustries SMC-1659-OVT magneto-optical cryostat allows variable-temperature (<1.5–300 K) and variable-field (0–7 T) operation and is positioned in the Faraday configuration. MCD intensities were measured as the absorbance difference $\Delta A = A_L - A_R$ (where L and R refer to left and right circularly polarized photons) and are reported as $\theta(\text{deg}) = 32.9\Delta A/A$. Band-edge Zeeman measurements were conducted on the same instrument in single-beam transmission mode by measuring $\text{Abs} = -\log(I/I_0)$. Variable-temperature variable-field magnetic susceptibility measurements were performed on powder samples of Co²⁺:ZnO using a Quantum Design MPMS SQUID magnetometer. The sample holder diamagnetism was subtracted from the raw magnetization data.

III. Results

Figure 1a shows absorption spectra collected every 30 s following addition of 30 μL (0.6 equiv) of ethanolic 0.554 M N(Me)₄OH to 250 μL of a 0.101 M solution of Zn(OAc)₂ in DMSO. Already by the first measurement (ca. 30 s following mixing), the spectrum is dominated by the distinctive band gap absorption feature of ZnO nanocrystals. With time, the band gap absorption feature grows, narrows, and shifts to lower energy. Plots of the band gap absorption intensity and energy versus time are provided in the Supporting Information (Figure S1). These data demonstrate that the system reaches a metastable state after ca. 10 min. The band shape narrowing observed in Figure 1a reveals size distribution focusing, which arises from size-dependent growth kinetics. Subsequent growth by Ostwald ripening is observed on the day or week time scale at room temperature.

Figure 1b presents absorption spectra collected during addition of 0.2 equiv aliquots of 0.554 M N(Me)₄OH to a 0.101 M solution of Zn(OAc)₂ in DMSO. Addition of the first and second aliquots of N(Me)₄OH generates only broad, high-energy (>30 000 cm⁻¹) absorbance features. The 0.4 equiv spectrum shows signs of nucleation of small and inhomogeneous ZnO

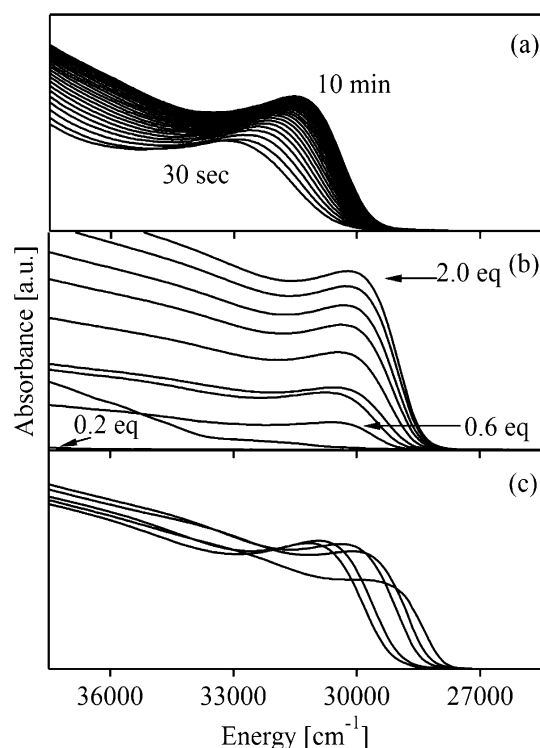


Figure 1. (a) Absorption spectra collected every 30 s between 30 s and 10 min following addition of 0.6 equiv of 0.554 M N(Me)₄OH to a 250 μL 0.101 M solution of Zn(OAc)₂ in DMSO. With time, the band gap absorption grows in intensity, narrows, and shifts to lower energy. (b) Absorption spectra collected during titration of 0.2 equiv aliquots of 0.552 M N(Me)₄OH to a 0.101 M DMSO solution of Zn(OAc)₂. (c) Absorption spectra collected during heating of ZnO QDs at 50 °C in DMSO. With heating (2, 5, 20, 40, and 120 min), the band gap transition shifts to lower energy.

nanocrystals. The formation of ZnO at this stage is verified by observation of the characteristic green ZnO trap luminescence. At 0.6 equiv, a strong absorption feature at 30 000 cm⁻¹ becomes apparent, readily associated with the first excitonic transition of ZnO. The average nanocrystal diameter estimated from this band gap energy is ca. 3.2 nm. Subsequent additions of N(Me)₄OH cause an increase in ZnO absorption intensity with little or no change in the energy of this feature, but the intensity increases are initially erratic and do not follow the added OH⁻ equiv linearly. Above ca. 1.0 equiv OH⁻, the increase in ZnO absorbance becomes linear with added N(Me)₄OH. Heating as-prepared ZnO nanocrystals in DMSO or TOPO leads to a slow decrease in band gap energy and intensity, indicative of slow particle growth by Ostwald ripening. Spectra collected periodically during this process in DMSO are presented in Figure 1c.

Figure 2 summarizes TEM data collected on aged pure ZnO nanocrystals having a band gap maximum of 29 500 cm⁻¹. The wide-area electron diffraction pattern (Figure 2c) shows only diffraction intensity associated with highly crystalline ZnO. The TEM images in Figure 2, parts a and d, verify the pseudo-spherical shapes and the high crystallinity of the particles. The average particle diameter determined from analysis of approximately 100 nanocrystals in this sample (Figure 2b) was 3.8 ± 0.6 nm, in good agreement with the average diameter of 3.8 nm estimated from the absorption spectrum of the same sample.

Figure 3 (top) shows color photographs of a reaction flask during addition of N(Me)₄OH to a DMSO solution of 98%

(17) Meulenkaamp, E. A. *J. Phys. Chem. B* **1998**, *102*, 5566–5572.

(18) van Dijken, A.; Meulenkaamp, E. A.; Vanmaekelbergh, D.; Meijerink, A. *J. Lumin.* **2000**, *90*, 123–128.

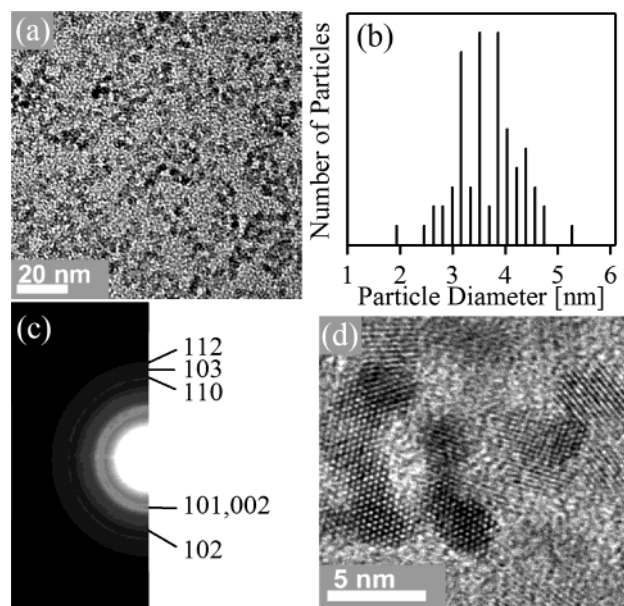


Figure 2. TEM data for pure ZnO QDs aged in DMSO. (a) Low-resolution TEM image. (b) Histogram computed for ~ 100 nanocrystals showing an average particle diameter of 3.8 ± 0.6 nm. (c) Wide-area electron diffraction image. (d) High-resolution TEM image.

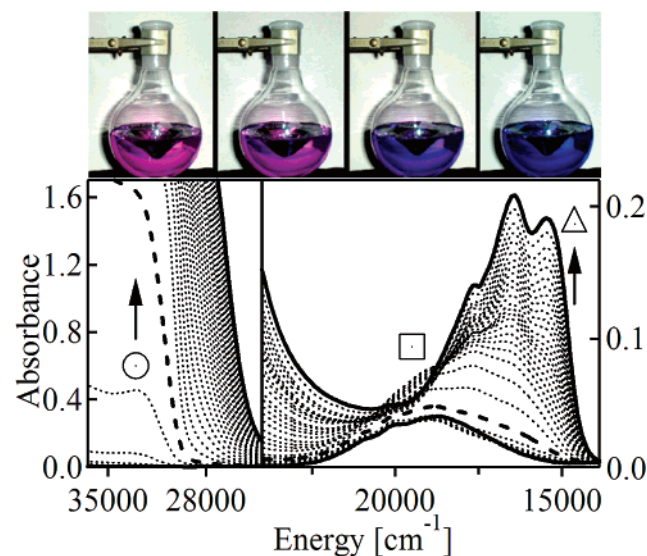


Figure 3. Top: Photographs taken during the preparation of $\text{Co}^{2+}:\text{ZnO}$ DMS-QDs as described in the text. The DMSO solution changes from pink to blue with addition of base, indicative of the conversion of octahedral Co^{2+} to tetrahedral Co^{2+} . Bottom: Electronic absorption spectra in the ZnO band gap (left) and Co^{2+} ligand-field (right) energy regions collected with titration of 0.2 equiv aliquots of $\text{N}(\text{Me})_4\text{OH}$ to a DMSO solution of 98% $\text{Zn}(\text{OAc})_2/2\%$ $\text{Co}^{2+}(\text{OAc})_2$. The band gap (\circ), intermediate Co^{2+} ligand field (\square), and substitutionally doped $\text{Co}^{2+}:\text{ZnO}$ ligand-field (Δ) intensities are indicated.

$\text{Zn}(\text{OAc})_2/2\%$ $\text{Co}(\text{OAc})_2$ under conditions identical to those used in Figure 1b for pure ZnO. The first panel, collected prior to base addition, shows the characteristic pink color of octahedral Co^{2+} . Base addition causes the solution to turn from pink to blue. Figure 3 (bottom) shows absorption spectra collected in the visible and UV energy regions during the course of the same procedure. Prior to $\text{N}(\text{Me})_4\text{OH}$ addition, only the weak absorption of the Co^{2+} precursor species is observed, centered at $19\,000\text{ cm}^{-1}$. As in Figure 1b, addition of $\text{N}(\text{Me})_4\text{OH}$ leads to growth of a strong ZnO band gap absorption feature in the UV (Figure 3, bottom left). This transition is too intense to be

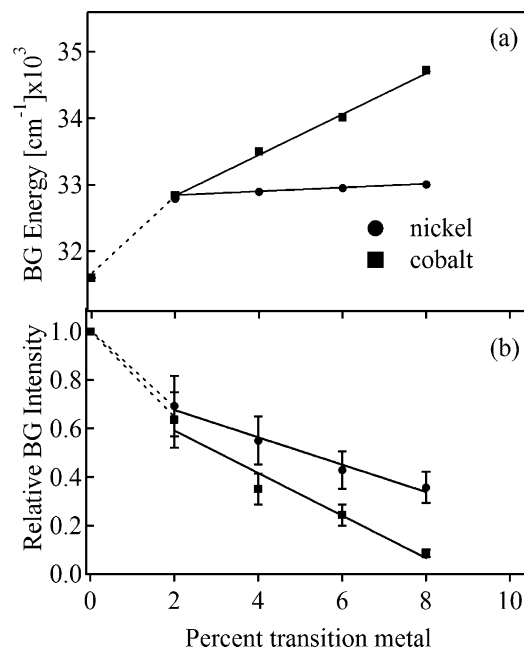


Figure 4. ZnO band gap (a) energies and (b) absorption intensities measured after addition of 0.66 equiv of 0.554 M $\text{N}(\text{Me})_4\text{OH}$ to a 250 μL 0.101 M solution of $\text{TM}(\text{OAc})_2$ in DMSO containing the indicated percentage of Ni^{2+} or Co^{2+} . The error bars in (a) are the size of the data points. The solid lines are linear best fits to the data with nonzero dopant concentrations. The dashed lines are guides to the eye.

observed on the same sensitivity scale as the visible transitions. Notably, at the end of the procedure the energy of the band gap transition is greater in the Co^{2+} -doped sample (Figure 3, $33\,000\text{ cm}^{-1}$) than in the pure ZnO QDs prepared under identical conditions (Figure 1b, $30\,000\text{ cm}^{-1}$). In the ligand-field energy region (Figure 3, bottom right), addition of up to 0.3 equiv of $\text{N}(\text{Me})_4\text{OH}$ has no apparent effect on the Co^{2+} visible absorption spectrum. The first changes are observed only after addition of ca. 0.35 equiv of $\text{N}(\text{Me})_4\text{OH}$, after which the growth of a broad feature with a maximum at ca. $17\,500\text{ cm}^{-1}$ becomes apparent. The change in Co^{2+} absorbance is correlated with the appearance of the ZnO band gap absorption. This broad Co^{2+} absorbance feature increases until 0.6 equiv of base have been added, and it then decreases with further base addition. Above ca. 0.45 equiv of added $\text{N}(\text{Me})_4\text{OH}$, a new structured feature with a central peak at $16\,500\text{ cm}^{-1}$ begins to appear in proportion to the quantity of $\text{N}(\text{Me})_4\text{OH}$ added. The interdependence of these two Co^{2+} absorption signals is apparent from the isosbestic points at $18\,550\text{ cm}^{-1}$ and $20\,750\text{ cm}^{-1}$ in the complete $\text{N}(\text{Me})_4\text{OH}$ titration data set shown in Figure 3.

Figure 4 summarizes the results of absorption measurements performed over a range of dopant concentrations. The metastable ZnO band gap energies and intensities, averaged over three independent measurements, are plotted as a function of initial metal ion concentration in Figure 4, parts a and b, respectively. The metastable band gap energy of $\text{Co}^{2+}:\text{ZnO}$ increases linearly as the initial Co^{2+} concentration increases, and the band gap intensity is inversely proportional to the Co^{2+} concentration. Similarly, the $\text{Ni}^{2+}:\text{ZnO}$ band gap energy increases with introduction of Ni^{2+} , but further increases in initial Ni^{2+} mole percent above 1% have little effect on the ZnO band gap energy. The trend observed for the dependence of the band gap intensity on initial Ni^{2+} concentration is similar to that observed for Co^{2+} doping.

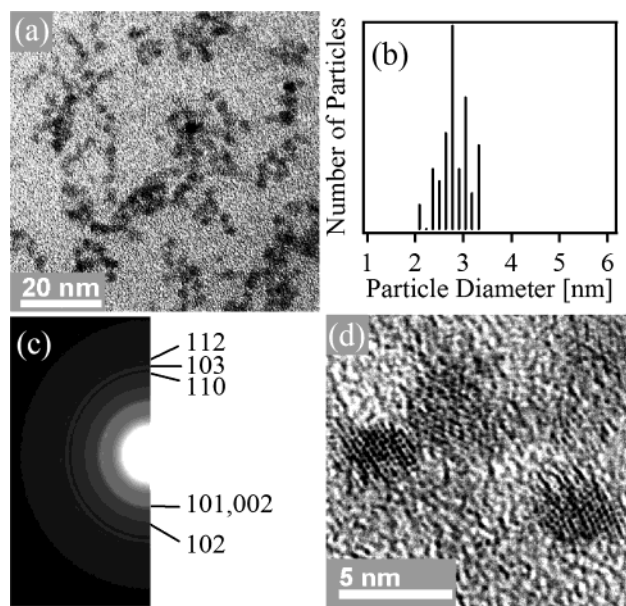


Figure 5. TEM data for 5% Co²⁺:ZnO nanocrystals prepared in DMSO. (a) Low-resolution TEM image. (b) Histogram computed for ~100 nanocrystals showing an average particle diameter of 2.9 ± 0.3 nm. (c) Wide-area electron diffraction image. (d) High-resolution TEM image.

Figure 5 shows the results from TEM measurements of ~5% Co²⁺-doped ZnO nanocrystals as grown from DMSO. Because of the low vapor pressure of DMSO, these nanocrystals were precipitated from DMSO with ethyl acetate and resuspended in EtOH, from which they could be deposited onto the graphite TEM substrate. Figure 5a presents an overview image showing ca. 30 nanocrystals. The nanocrystals are of nearly spherical shape. Figure 5b shows a histogram of nanocrystal sizes for a population of ca. 100 isolated crystals and reveals a fairly uniform ensemble of nanocrystals with an average diameter of 2.9 ± 0.3 nm. This diameter is in good agreement with that estimated optically for this sample (2.8 nm). The wide-area electron diffraction pattern obtained from this sample (Figure 5c) is indicative of highly crystalline wurtzite ZnO. Figure 5d shows a high-resolution image of several of these nanocrystals and confirms their high crystallinity and uniform sizes and shapes.

The low-temperature absorption and MCD spectra of a frozen solution of 5 nm diameter 1.7% Co²⁺:ZnO quantum dots are shown in Figure 6a. Centered at $15\,900\text{ cm}^{-1}$ is the richly structured ${}^4A_2 \rightarrow {}^4T_1(P)$ ligand-field transition of the substitutionally doped Co²⁺ ions, with minor contributions from several nearby doublets as described previously.^{19,20} Integration of the ligand-field absorption intensity yields an oscillator strength of $f = 2.0 \times 10^{-3}$ for this transition. This value is smaller than but comparable to that reported for bulk Co²⁺:ZnO ($f = 5.0 \times 10^{-3}$).¹⁹ The band gap absorbance tails into the visible without inflection, even at low temperature. The MCD spectrum of the same Co²⁺:ZnO QDs shows both the ligand-field and band gap transitions at the same energies as observed in the absorption spectrum. A broad sub-bandgap transition with a negative MCD peak maximum at ca. $25\,200\text{ cm}^{-1}$ is also observed. The MCD intensity across the entire spectral range increases uniformly with increasing magnetic field or decreasing temperature, indicating that all transitions arise from the same magnetic chromophore.

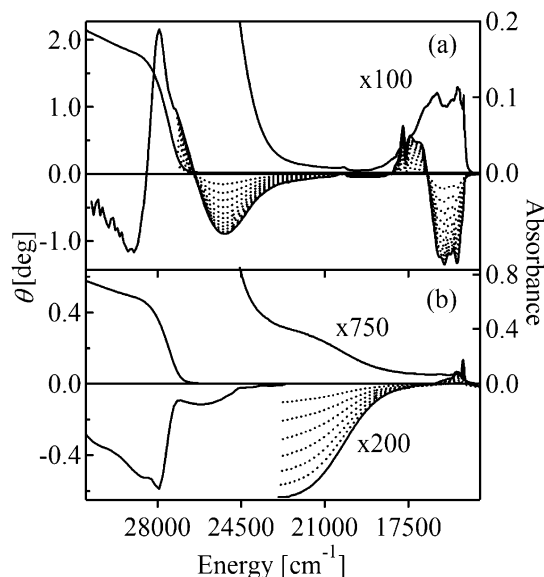


Figure 6. 7 K absorption and 5 K variable-field (0–6.5 T) MCD spectra of (a) 1.7% Co²⁺:ZnO nanocrystals and (b) 1.5% Ni²⁺:ZnO nanocrystals.

The intensities of the major features in the MCD spectrum of Co²⁺:ZnO from Figure 6a, corrected for saturation effects, are parametrized in Table 1 by their C_0/D_0 ratios, defined in eq 1:²¹

$$\frac{C_0}{D_0} = \frac{kT}{\beta H} \left(\frac{\Delta\epsilon}{\epsilon} \right) \quad (1)$$

Here, $k = 0.69503\text{ cm}^{-1}/\text{K}$, T is the temperature (K), β is $0.46686\text{ cm}^{-1}/\text{Tesla}$, H is the applied field (Tesla), $\Delta\epsilon$ is the molar ellipticity, and ϵ is the molar absorption coefficient. The pseudo-A MCD feature of the band gap transition in Co²⁺:ZnO DMS-QDs shows a C_0/D_0 ratio approximately 100 times smaller than that of the Co²⁺ ${}^4A_2 \rightarrow {}^4T_1(P)$ ligand-field transition.

The 5 K MCD and 7 K absorption spectra of a thin film of TOPO-treated 4.0 nm diameter 1.5% Ni²⁺:ZnO QDs are shown in Figure 6b. Three distinct spectral regions are identified in both the absorption and MCD spectra: ligand field ($15\,160\text{--}16\,300\text{ cm}^{-1}$), charge transfer ($19\,400\text{--}25\,300\text{ cm}^{-1}$), and band gap ($26\,000\text{--}28\,000\text{ cm}^{-1}$). MCD intensities in each of these three regions show the same temperature and field dependence, confirming their origin in the same magnetic chromophore. Temperature-independent B_0/D_0 ratios (eq 2²¹) for prominent features are included in Table 1.

$$\frac{B_0}{D_0} = \frac{1}{\beta H} \left(\frac{\Delta\epsilon}{\epsilon} \right) \quad (2)$$

The band gap rotational strength of the Ni²⁺:ZnO QDs is approximately an order of magnitude smaller than that of the Co²⁺:ZnO QDs. As a consequence, data in the band gap spectral region could not be obtained on the same thickness sample as used for the lower-energy regions and are generally of poorer quality. Figure 7 shows high-resolution absorption and MCD spectra of the same Co²⁺:ZnO and Ni²⁺:ZnO DMS-QD samples used in Figure 6. The spectra show rich fine structure with transition full-widths-at-half-max as small as 30 cm^{-1} .

(20) Koidl, P. *Phys. Rev. B* **1977**, *15*, 2493–2499.

(21) Piepho, S. B.; Schatz, P. N. *Group Theory in Spectroscopy with Applications to Magnetic Circular Dichroism*; Wiley: New York, 1983.

(19) Weakliem, H. A. *J. Chem. Phys.* **1962**, *36*, 2117–2140.

Table 1. MCD Intensities of Prominent Features in the Spectra of $\text{Co}^{2+}:\text{ZnO}$ and $\text{Ni}^{2+}:\text{ZnO}$ DMS-QDs, Parameterized by Their C_0/D_0 (Co^{2+}) or B_0/D_0 (Ni^{2+}) Ratios As Defined in Eqs 1 and 2

transition	$\text{Co}^{2+}:\text{ZnO}$		$\text{Ni}^{2+}:\text{ZnO}$	
	C_0/D_0	energy (cm^{-1})	B_0/D_0	energy (cm^{-1})
ligand field	3.6×10^{-1}	15 432	5.7×10^{-2}	15 163
charge transfer	8.1×10^{-2a}	25 000 ^a	1.6×10^{-2}	23 000
band gap	3.2×10^{-3}	28 000	8.8×10^{-4}	28 000

^a Because of overlap with the band-gap onset, precise absorption and MCD energies and intensities of this transition are difficult to measure reliably, and the C_0/D_0 ratio is considered approximate.

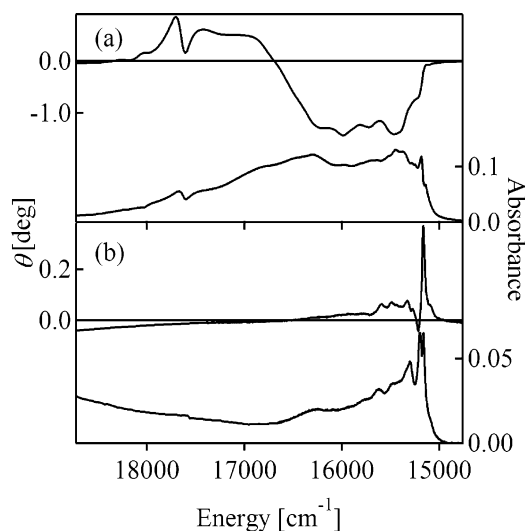


Figure 7. High-resolution 7 K absorption and 5 K, 7 T MCD spectra of (a) 1.7% $\text{Co}^{2+}:\text{ZnO}$ and (b) 1.5% $\text{Ni}^{2+}:\text{ZnO}$ nanocrystals from Figure 6.

Figure 8a shows the $\text{Co}^{2+}:\text{ZnO}$ MCD intensity measured at 15 700 cm^{-1} (ligand field) and 27 200 cm^{-1} (band gap onset) as a function of field at 5 and 10 K. The intensity saturates at high fields and low temperatures, consistent with C-term MCD behavior. Figure 8b shows the $\text{Ni}^{2+}:\text{ZnO}$ MCD intensity measured at 15 165 cm^{-1} as a function of field at several temperatures between 5 and 80 K. The intensity does not saturate at high fields and low temperatures and is temperature-independent up to ca. 40 K for a given field.

Figure 9b plots the energy of the ZnO band edge as a function of applied magnetic field, relative to its energy at zero field, measured at 5 K. The band edge shifts to lower energy as the field is increased by an average amount of 53 cm^{-1}/T over the range of 0–7 T. The response is not linear with field, however, and shows a distinct turning point between 1 and 3 T. Between 3 and 7 T, the field dependence is larger than the average value, and is ca. 65 cm^{-1}/T . The solid lines are the results of analysis described in Section IV.D.iii.

Figure 10 presents the results of magnetic susceptibility measurements on 5.0-nm diameter 3.6% $\text{Co}^{2+}:\text{ZnO}$ DMS-QDs that have been allowed to aggregate into the dense micron-dimensioned gel structures shown in the SEM image (Figure 10b, inset). The 300 K magnetization data (Figure 10a) are dominated by a magnetic hysteresis having coercivity of 105 Oe and remanence of 0.465×10^{-3} emu/g. The 300 K saturation moment is 2.56×10^{-3} emu/g. The properties of the hysteresis depend only weakly upon temperature and no evidence of the Curie temperature is observed up to 350 K, the instrument limit.

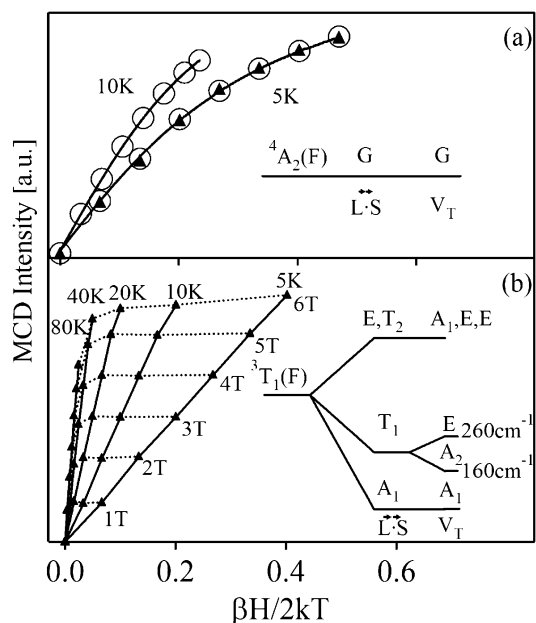


Figure 8. Variable-temperature, variable-field MCD intensities (a) collected at 15 600 cm^{-1} (O, Co^{2+} ligand-field region) and 27 200 cm^{-1} (\blacktriangle , band gap region) for the 1.7% $\text{Co}^{2+}:\text{ZnO}$ nanocrystals from Figure 6a and (b) collected at 15 400 cm^{-1} (Ni^{2+} ligand-field region) for the 1.5% $\text{Ni}^{2+}:\text{ZnO}$ nanocrystals from Figure 6b. The solid and dashed lines are guides to the eye. Insets: Ground-state energy level splittings of tetrahedral Co^{2+} in ZnO and Ni^{2+} in ZnO under the actions of first-order spin-orbit coupling ($L \cdot S$) and a weak trigonal low-symmetry distortion (V_T).

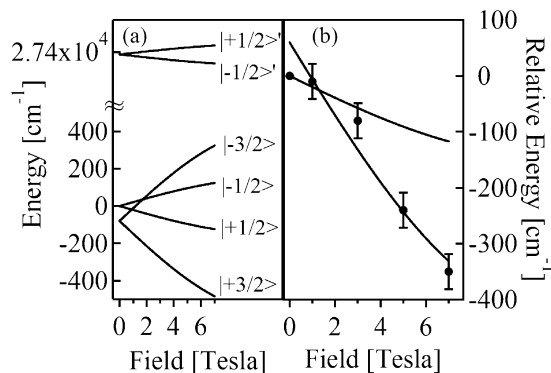


Figure 9. (a) Zeeman splitting pattern for the one-electron band levels of ZnO DMSs with $H||z$. (b) Experimental band edge Zeeman shift for the 1.7% $\text{Co}^{2+}:\text{ZnO}$ DMS-QDs used in Figure 6a. The solid lines represent the transition energies predicted from the Zeeman splittings for ZnO shown in (a) using $N_0\beta = -2.3$ eV ($-18\,500$ cm^{-1}) as described in the text.

IV. Analysis and Discussion

A. Synthesis of ZnO Quantum Dots in DMSO. Our procedure for the synthesis of ZnO and doped ZnO quantum dots involves addition of OH^- into a DMSO solution of $\text{Zn}(\text{OAc})_2$ to form nanocrystals by hydrolysis and condensation. Absorption measurements as a function of time after addition of 0.6 equiv of OH^- (Figure 1a) show rapid nucleation and subsequent growth of the ZnO nanocrystals and demonstrate that the reaction reaches a metastable state after approximately 10 min, after which it slowly Ostwald ripens. Absorption spectra measured during stepwise titration of OH^- are extremely informative about the mechanistic aspects of this synthesis. Under our experimental conditions, initial addition of 0.2 equiv of OH^- does not lead to ZnO nucleation but does give rise to a small change in the absorption spectrum at high energies

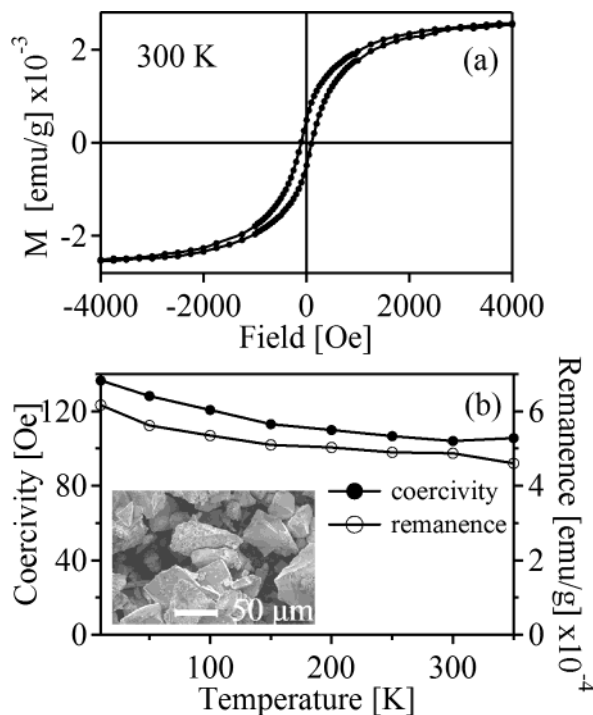


Figure 10. (a) 300 K magnetic hysteresis loop and (b) hysteresis coercivity and remanence temperature dependence collected on a powder sample of 3.6% Co²⁺:ZnO DMS-QD aggregates (inset).

(Figure 1b). We attribute this behavior to the formation of basic zinc acetate molecular clusters. Discrete clusters such as Zn₄O(OAc)₆ and Zn₁₀O₄(OAc)₁₂ have been identified in basic zinc acetate solutions formed in ethanol,²² and it is likely that similar structures are also formed in DMSO. These molecular clusters are precursors to ZnO nucleation.²²

After addition of 0.4 equiv of OH⁻, ZnO nucleation occurs and gives rise to a band gap absorption feature centered at 32 500 cm⁻¹. The assignment of this feature to crystalline ZnO is supported by the observation of the characteristic green surface-trap emission of ZnO with excitation into this band (data not shown). Assuming pseudospherical crystallites, this band gap energy corresponds to nanocrystal diameters of ca. 2 nm.^{17,18} Addition of more base causes growth and further nucleation of ZnO, as evidenced by the decrease in the energy of the band gap transition to 30 000 cm⁻¹ (diam ≈ 3.2 nm) and the increase in the band gap absorbance, respectively. The minimum band gap energy obtained is 30 000 cm⁻¹, indicating that growth from solution beyond diam ≈ 3.2 nm is not competitive with the nucleation and growth of new crystallites under these conditions. TEM images of pure ZnO nanocrystals allowed to ripen for 2 days at room temperature in DMSO show nearly spherical crystallites of fairly uniform size, and electron and X-ray powder diffraction measurements confirm their identity as highly crystalline wurtzite ZnO (Figure 2). Ostwald ripening can be accelerated by gentle heating of the DMSO solution at 50 °C, as shown in Figure 1c. This procedure thus generates highly crystalline colloidal ZnO QDs.

B. Synthesis of Transition-Metal-Doped ZnO QDs in DMSO. The same procedure described above can be used to

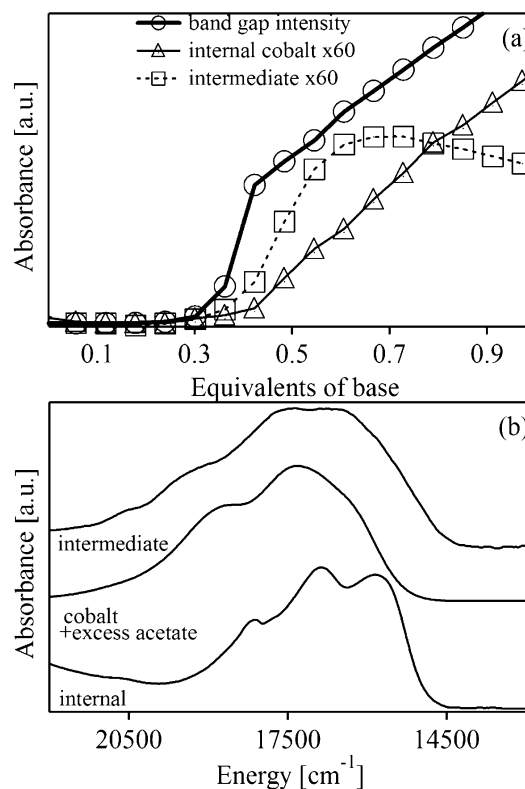
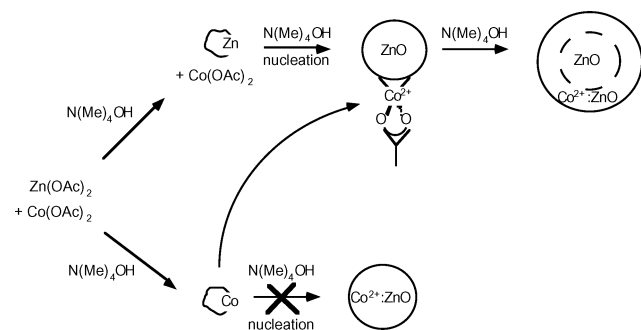


Figure 11. (a) Absorbance values obtained from single-value decomposition analysis of the data from Figure 3. The band gap (○), intermediate Co²⁺ ligand-field [□], and internal Co²⁺:ZnO ligand-field (△) intensities are plotted vs equivalents of base added during synthesis. (b) Deconvolved ligand-field absorption spectrum of the intermediate compared to the ligand-field spectra of Co²⁺ in DMSO with excess acetate and of substitutionally doped Co²⁺:ZnO prepared in DMSO and treated with TOPO.

synthesize transition-metal-doped ZnO QDs. We focus here on the synthesis of Co²⁺- and Ni²⁺-doped nanocrystals. Our results for other dopants will be reported separately. Using Co²⁺ as the dopant, base addition converts the pale pink starting solution into a deep blue solution (Figure 3, top). The pink color arises from the ⁴T_{1g}(F) → ⁴T_{1g}(P) and ⁴T_{1g}(F) → ⁴A_{2g} ligand-field transitions (centered at 19 000 cm⁻¹, Figure 3, bottom) of pseudo-octahedral Co²⁺ ions likely coordinated by one or more DMSO molecules under these conditions. The blue color arises from the intense ⁴A₂ → ⁴T₂(P) ligand-field absorption band (maximum at ca. 16 500 cm⁻¹, Figure 3, bottom) of Co²⁺ ions in the tetraoxo cation coordination environment of wurtzite ZnO.^{13,19} Greater insight is obtained by representing these titration data as intensities of the deconvolved features versus base addition (Figure 11a). Analogous to the data in Figure 1b, nucleation of ZnO occurs only after addition of ca. 0.4 base equiv, at which point a sharp increase in absorbance in the ZnO band gap region is observed. The band gap intensity increases stoichiometrically with subsequent base additions, indicating further ZnO nucleation with each titrated increment. Extrapolation of the slope of the line formed by plotting band gap intensity (i.e., nanocrystal concentration) vs added base equiv very nearly intersects the origin, indicating that the majority of base added has been consumed to form ZnO. This conclusion implies that only a small fraction of added base exists in the form of molecular precursors during the later stages of synthesis, consistent with the low oxygen content of the basic zinc acetate precursors identified previously.²² Importantly, there is no sharp

(22) (a) Schmidt, T.; Mueller, G.; Spanhel, L.; Kerkel, K.; Forchel, A. *Chem. Mater.* **1998**, *10*, 65–71. (b) Spanhel, L.; Anderson, M. A. *J. Am. Chem. Soc.* **1991**, *113*, 2826–2833. (c) Tokumoto, M. S.; Briois, V.; Santilli, C. V.; Pulcinelli, S. H. *J. Sol.-Gel Sci. Technol.* **2003**, *26*, 547–551.

Scheme 1



increase in the absorbance associated with substitutional Co²⁺ concomitant with that observed for the ZnO band gap absorption. Instead, the absorption signal of the substitutionally doped ions grows in stoichiometrically with each base addition after ZnO nucleation has occurred. Extrapolation of these intensities plotted in Figure 11a does not go through the origin but intersects zero intensity at 0.36 equiv of base, very nearly where crystalline ZnO is first observed. These data clearly indicate that the initial ZnO nucleation event does not incorporate Co²⁺ dopants.

Also evident from the data in Figure 3 is the formation and decay of a broad intermediate absorption band centered at ca. 19 000 cm⁻¹, the intensity of which is plotted in Figure 11a vs base addition. Like that of substitutional Co²⁺, this absorption feature appears only after nucleation of ZnO nanocrystals and also shows no initial jump in intensity. The isosbestic points in the titration data set at 18 550 and 20 750 cm⁻¹ reveal that this species is the direct precursor to substitutionally doped Co²⁺. The spectrum of this intermediate, deconvolved by single-value decomposition of the full titration data set, is shown in Figure 11b in comparison with that of substitutionally doped Co²⁺:ZnO. Its higher energy reveals a greater average ligand-field strength, and its breadth suggests inhomogeneous speciation. Together, the titration and band shape data suggest that this intermediate signal arises from Co²⁺ ions bound to the surfaces of ZnO nanocrystals. A similar absorption spectrum has been obtained by deliberate binding of Co²⁺ to ZnO nanocrystal surfaces in EtOH, where the surface-bound Co²⁺ ions likely have acetate terminal ligation.¹³ The visible ligand-field absorption spectrum of Co²⁺ in DMSO in the presence of excess acetate is included in Figure 11b for comparison. This spectrum is energetically similar to that of the intermediate but is somewhat narrower, verifying the stronger ligand-field strength of acetate than of the ZnO lattice oxides and the propensity for acetates to support the tetrahedral Co²⁺ geometry.

From the data in Figures 3 and 11 just described, we conclude that Co²⁺ ions in solution remain octahedrally coordinated until the nucleation of ZnO crystallites, at which point they bind to the nanocrystal surfaces in tetrahedral geometries either as monomers or within basic acetate clusters. Subsequent reaction with OH⁻ liberates acetate and yields substitutionally doped Co²⁺ ions in ZnO. These mechanistic conclusions are summarized in Scheme 1.

The absence of Co²⁺ ions in the initially nucleated ZnO cores is an important observation of general significance to the field of crystallization.²³ It reveals that ZnO nucleation is sensitive

to the chemical properties of transition-metal impurities. This sensitivity can be studied quantitatively by comparison of ZnO band gap intensities (which are approximately proportional to QD concentrations) measured from syntheses with and without dopants under otherwise identical conditions. The data in Figure 4b show that the number of nucleated nanocrystals depends very strongly on the initial dopant ion concentration. Addition of 2% Co²⁺ or Ni²⁺ ions to the starting solution, for example, results in the formation of ca. 35% fewer nanocrystals, and the effect increases as the dopant concentration is increased. Fitting these data to linear functions (solid lines in Figure 4b) yields slopes of $m = -9\%$ nucleation/% Co²⁺ and -6% nucleation/% Ni²⁺, respectively, with slightly larger values for the initial TM²⁺ addition. As a control, we have performed similar measurements in which only the base concentration is varied. Reduced base concentration also reduces the number of nucleated nanocrystals, but the effect is ca. 20 times smaller than that observed for TM²⁺ addition. This result indicates that the influence of TM²⁺ dopants on crystal nucleation does not simply arise from consumption of OH⁻ by the dopant in solution. Rather, it is concluded that the impurity ions directly inhibit the nucleation of ZnO nanocrystals.

The strong dependence of nucleation on small TM²⁺ concentrations is attributed to the incorporation of TM²⁺ ions into the basic acetate cluster precursors. As described above, Figure 3 shows that tetrahedral Co²⁺ is not formed prior to ZnO nucleation, and therefore, Co²⁺ ions in the basic acetate precursors must retain their pseudo-octahedral coordination geometries. Nucleation of ZnO from precursors containing Co²⁺ is consequently slowed by the added barrier associated with conversion of Co²⁺ ions from octahedral to tetrahedral geometries. Perhaps more important, however, is the fact that some of the driving force for crystal nucleation is sacrificed upon the introduction of an impurity. The data in Figure 4a show that the metastable ZnO band gap energies obtained in the presence of Co²⁺ or Ni²⁺ are significantly greater than those obtained for pure ZnO nanocrystals made under otherwise identical conditions, and therefore, that the resulting nanocrystal dimensions are reduced upon doping. TEM measurements of Co²⁺:ZnO QDs (e.g., Figure 5) verify the average diameters estimated spectroscopically. These differences cannot be explained in terms of kinetic effects, but must reflect a thermodynamic barrier to further growth of ZnO around a doped nanocrystal, or equivalently, a greater solubility of Co²⁺-doped ZnO nanocrystals than of pure ZnO nanocrystals. This can be related to the Gibbs–Thompson effect²⁴ and described using eq 3, where S_r is the solubility of a crystallite of radius r , S_B is the solubility of the corresponding bulk material, V_m is the molar volume, and σ is the specific surface energy of the nanocrystal.

$$S_r = S_B \exp\left[\frac{2\sigma V_m}{rRT}\right] \quad (3)$$

Surface or near-surface dopants cause lattice strain that elevates the specific surface energies, σ , and, hence, increases the crystallite solubility. The thermodynamic lattice destabilization by dopants observed to affect the metastable nanocrystal diameters in Figure 4a is also responsible for the absence of

(23) Oxtoby, D. W. *Acc. Chem. Res.* **1998**, *31*, 91–97.

(24) (a) Davis, K. J.; Dove, P. M.; De Yoreo, J. J. *Science* **2000**, *290*, 1134–1137. (b) van Enkevort, W. J. P.; van der Berg, A. C. J. F.; Kreuwel, K. B. G.; Derksen, A. J.; Couto, M. S. *J. Cryst. Growth* **1996**, *166*, 156–161.

directly nucleated Co²⁺:ZnO from Co²⁺-containing precursors, since this destabilization shifts the critical nucleation radius (above which a nucleated crystallite will grow rather than dissolve) for doped ZnO to larger dimensions than that of undoped ZnO.²³ As shown in Figure 11, the only nuclei that survive under our experimental conditions are consequently those that do not contain impurities.

C. Postsynthetic Processing of QDs. We have explored various procedures for isolation of ZnO DMS-QDs from DMSO. One method, mentioned above, entails precipitation with ethyl acetate and resuspension in EtOH. We have also previously shown that the isocrystalline core/shell (ICS) procedure, which involves epitaxial growth of pure ZnO shells around ZnO DMS-QDs in EtOH, is an effective method for ensuring completely internally doped DMS-QDs.^{13,14} In this study, we report our recent finding that gentle heating of ZnO DMS-QDs in TOPO is also effective in eliminating surface-bound dopants, in this case by their solvation.¹⁶ Ligand-field absorption spectra collected periodically during the TOPO treatment show that dopants are effectively removed from the surfaces of ZnO nanocrystals (Supporting Information, Figure S2), yielding DMS-QDs with only the internally doped impurity ions remaining. The dopant homogeneity obtained by this procedure appears to be slightly greater than that obtained from the ICS procedure, giving rise to somewhat better resolved absorption and MCD spectra. If not already ripened in DMSO, the high temperature of the TOPO treatment also accelerates Ostwald ripening and increases the nanocrystal diameters. Representative TEM data for TOPO-treated nanocrystals is included in the Supporting Information (Figure S3). TOPO-treated ZnO DMS-QDs prepared in this way are well suited for subsequent solution manipulation and processing and have been used for spin-coating the high optical-quality films used in our spectroscopic studies (Section IV.D.).

D. Optical, Magneto-Optical, and Magnetic Properties. As described in sections IV.A and IV.B, ligand-field absorption spectroscopy is a powerful analytical tool that allows direct observation of the dopant ions themselves during synthesis of DMS nanocrystals, and can therefore be used for evaluation and refinement of synthetic methodologies. A central motivation for synthesizing high-quality DMS-QDs is the exploration of fundamental electronic structure/function relationships in this class of materials. In this section, we describe the use of low-temperature absorption and MCD spectroscopies as electronic structural probes of the DMS-QDs synthesized as described above. The intrinsic optical electronic transitions of DMSs fall into three broad classifications: ligand-field, charge-transfer (CT), and semiconductor band-to-band transitions. Each type of transition provides complementary information about the electronic structure of the DMS as a whole that we then relate to the spintronics-relevant functional properties of these materials.

(i) Ligand-Field Transitions. The ⁴A₂ → ⁴T₁(P) ligand-field transition of substitutionally doped Co²⁺ in wurtzite ZnO is observed at low energies in the overview absorption and MCD spectra shown in Figure 6a. This energy region is shown on an expanded scale in Figure 7a. The rich, fine structure of the ⁴A₂ → ⁴T₁(P) transition arises from many sources and has been addressed in detail previously through high-resolution absorption spectroscopy on low-doped bulk Co²⁺:ZnO single crystals.^{19,20,25} For our purposes, we note that the fine structure observed in

these quantum-confined nanocrystals agrees quantitatively to within ~1 cm⁻¹ with that reported for bulk single crystals of Co²⁺:ZnO across the entire ⁴T₂(P) multiplet.^{19,20,26} This agreement clearly indicates that quantum confinement effects on the energies of these ligand-field transitions are negligible and, hence, that the wave functions involved in the ligand-field transitions are highly localized on the dopant ions. This excellent agreement also demonstrates the homogeneity of substitutional doping in these nanocrystals.

The ⁴A₂ → ⁴T₁(P) ligand-field transition gives rise to an intense pseudo-A term feature in the MCD spectrum, with intensity arising predominantly from transitions to the four spinors of the split ⁴T₁(P) term. The signs and relative intensities of the ligand-field MCD intensities parallel those observed in CoCl₄²⁻ and other tetrahedral or pseudotetrahedral Co²⁺ ions.²⁷ Integration of the ligand-field MCD intensity reveals a small net violation of the intensity sum rule, indicative of a negative intensity contribution attributable primarily to spin-orbit coupling between the ⁴T₂(F) term and the ground state.²⁷

Extensive fine structure is also observed in the ³T₁(F) → ³T₁(P) ligand-field absorption and MCD spectra of Ni²⁺:ZnO QDs (Figure 7b). The ligand-field band is dominated by the trigonally split T₂ spinor component of the ³T₁(P),^{19,26,28} with A₁ and E trigonal components at 15 163 and 15 198 cm⁻¹ having full-widths-at-half-max of only ca. 30 cm⁻¹. These narrow bandwidths demonstrate a high degree of Ni²⁺ homogeneity in these DMS-QDs. These two electronic origins are oppositely signed in the MCD spectrum. At higher energies, overlapping electronic and vibronic MCD transitions broaden the fine structure. The net positive intensity in the ligand-field MCD spectrum offers a clear violation of the MCD sum rule and is attributed to the large spin-orbit coupling active within the ³T₁(F) ground term.

Emission spectra measured for pure ZnO QDs synthesized by our procedure are dominated by surface trap luminescence occurring in the visible spectral range and are very similar to those reported previously.¹⁸ Quantitative 300 K emission measurements show that >99% of this surface trap luminescence is quenched upon 2.0% Co²⁺ doping (Supporting Information, Figure S4), consistent with expectations based on the well-known role of Co²⁺ as a deep trap in II-VI semiconductors. Excitonic quenching is followed by rapid nonradiative relaxation to the ground state through the ligand-field manifold. No upper excited-state ligand-field emission is observed in our colloids at room temperature.^{28,29}

(ii) Charge-Transfer Transitions. The identification and assignment of sub-bandgap CT transitions in Co²⁺:ZnO and Ni²⁺:ZnO DMS-QDs are of interest because their energies and intensities relate to the sp-d exchange interactions that govern the magnetism and magneto-optical properties of this class of materials. The broad sub-bandgap transition observed between ca. 18 000 and 23 000 cm⁻¹ in the absorption spectrum of Ni²⁺:ZnO (Figure 6b) has been assigned previously on the basis of

(25) We note the observation of a prominent Fano antiresonance dip at 17 700 cm⁻¹ in the MCD spectrum of Co²⁺:ZnO. The weaker dip in the absorption spectrum at the same energy has previously been attributed to the ²A₁(G) state.²⁰

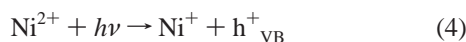
(26) Anderson, R. S. *Phys. Rev.* **1967**, *164*, 398–405.

(27) Denning, R. G.; Spencer, J. A. *Symp. Faraday Soc.* **1970**, 84–91.

(28) Schulz, H. J.; Thiede, M. *Phys. Rev. B* **1987**, *35*, 18–34.

(29) ⁴T₁(P) emission in bulk Co²⁺:ZnO single crystals is observed only at cryogenic temperatures (*T* < 5 K reported) and with low quantum yields.²⁸

single-crystal polarized absorption data as a charge-transfer transition in which the Ni^{2+} acts as the CT acceptor and the valence band serves as the CT donor.^{19,30} If we treat the semiconductor nanocrystal as a ligand to the dopant ion, this transition falls into the broad classification of a ligand-to-metal charge-transfer (LMCT) transition. A similar transition is observed in $\text{Ni}^{2+}:\text{ZnS}$ and has been assigned in the same way on the basis of high-resolution absorption, photoluminescence excitation, and Zeeman data.^{30,31} In both $\text{Ni}^{2+}:\text{ZnO}$ and $\text{Ni}^{2+}:\text{ZnS}$, the LMCT excited state can be described as comprising a central Ni^+ ion and an electrostatically bound hole from the valence band having a hydrogen-like wave function.



In contrast, no discrete charge-transfer transition can be identified in the absorption spectrum of $\text{Co}^{2+}:\text{ZnO}$, even at low temperatures.¹⁹ $\text{Co}^{2+}:\text{ZnO}$ does, however, exhibit substantially more absorption intensity tailing into the visible from the band gap maximum than does pure ZnO. Clear evidence of a charge-transfer transition in $\text{Co}^{2+}:\text{ZnO}$ comes from the MCD spectrum (Figure 6a), in which an intense negative sub-bandgap MCD feature is observed that increases in intensity up to 25 200 cm^{-1} before being occluded by the overlapping positive band gap transition. Because of overlap with the band gap transition, the value of 25 200 cm^{-1} is considered to be a lower limit for the band maximum of this negative MCD transition. This transition carries too much absorption intensity (Figure 6a) to be assigned as one of the spin-forbidden Co^{2+} ligand-field excitations also anticipated in this energy region. This broad MCD band and the corresponding tailing absorption intensity are instead assigned as a CT transition. This assignment is supported by the relatively small C_0/D_0 ratio estimated for this band in Table 1. Experimentally, C_0/D_0 ratios are typically up to an order of magnitude smaller for CT transitions than for ligand-field transitions,³² and the values shown in Table 1 are thus consistent with this assignment.

The specific nature of this CT transition in $\text{Co}^{2+}:\text{ZnO}$ requires clarification. This intensity in thin-film bulk $\text{Co}^{2+}:\text{ZnO}$ has previously been assigned as a metal-to-ligand charge transfer (MLCT) transition,¹⁰ but its assignment as a LMCT transition appears more plausible. Although the LMCT and MLCT transitions may in fact both occur in this energy region in $\text{Co}^{2+}:\text{ZnO}$, we favor assignment of the absorption and negative MCD intensity at 25 200 cm^{-1} as arising from a LMCT transition based on comparison to $\text{Ni}^{2+}:\text{ZnO}$. The energies of the charge-transfer transitions observed in Co^{2+} - and Ni^{2+} -doped ZnO can be analyzed in terms of the different electronegativities and electronic configurations of the Ni^{2+} and Co^{2+} ions in the tetrahedral geometry.

As Jørgensen and others have observed,^{33,34} the energies of charge-transfer transitions are related to the electronegativities, χ , of the donor and acceptor moieties involved. For example,

the energies of the lowest LMCT transitions in the series of tetrahedral tetrahalide complexes CoX_4^{2-} ($\text{X}^- = \text{Cl}^-$, Br^- , and I^-) roughly scale with the differences in the ligand electronegativities. Similarly, for a fixed halide X^- , the first LMCT transition in NiX_4^{2-} consistently lies ca. 6600 cm^{-1} lower in energy than the corresponding transition in CoX_4^{2-} , largely due to the greater electronegativity of Ni^{2+} than that of Co^{2+} . Equation 5^{33,34} relates the charge-transfer transition energies to electronegativities on Pauling's electronegativity scale and further takes into account differences in spin-pairing energies (SPE) between the ground and excited electronic states.

$$E_{\text{LMCT}} = 30\,000\text{ cm}^{-1} \cdot [\chi_{\text{opt}}(L) - \chi_{\text{opt}}(M)] + \Delta\text{SPE} + 10\text{Dq} \quad (5)$$

The SPEs of the ground and CT excited electronic states can be estimated from the known electronic configurations and the Racah electron–electron repulsion parameters B and C (eq 6), determined spectroscopically from the ligand-field data.

$$\text{SPE} = [\langle S(S+1) \rangle - S(S+1)]D \quad (6a)$$

$$D = (7/6)[(5/2)B + C] \quad (6b)$$

For both tetrahedral Ni^{2+} and Co^{2+} , χ reflects the energy of the nonbonding (e) set of d orbitals, whereas a LMCT excitation would promote an electron into the σ^* -antibonding (t_2) set of d orbitals that lie at an energy of 10Dq above the nonbonding pair. Therefore, 10Dq is also included in eq 5.

The Ni^{2+} ligand-field spectroscopic data for both bulk and nanocrystalline $\text{Ni}^{2+}:\text{ZnO}$ are well accounted for by values of $\text{Dq} = 420\text{ cm}^{-1}$, $B = 770\text{ cm}^{-1}$, and $C/B = 4.8$.¹⁹ $\Delta\text{SPE} = +2/3D = +4370\text{ cm}^{-1}$ for this Ni^{2+} ion. Similarly, $\text{Dq} = 390$, $B = 775$, and $C/B = 4.5$ for Co^{2+} in ZnO ,¹⁹ and $\Delta\text{SPE} = +4/3D = 8440\text{ cm}^{-1}$. From the LMCT energies measured in the tetrahalide series, the difference in electronegativities of Ni^{2+} and Co^{2+} is accurately determined to be $\Delta\chi_{\text{opt}}(\text{Ni}^{2+} - \text{Co}^{2+}) = 0.1$. Values of $\chi_{\text{opt}}(\text{Ni}^{2+}) \approx 2.0$ and $\chi_{\text{opt}}(\text{Co}^{2+}) \approx 1.9$ are estimated.^{34,35} These χ_{opt} values are remarkably constant over a diverse set of ligands and should be applicable in the present case as well. With the above numbers, solution of eq 5 for the energy difference between the LMCT transitions of $\text{Co}^{2+}:\text{ZnO}$ and $\text{Ni}^{2+}:\text{ZnO}$ yields a value of ca. 6770 cm^{-1} , as anticipated from the tetrahalide series. From the onset of the LMCT transition (estimated as the energy at which the CT intensity equals that of the ligand-field maximum) of $E_{\text{LMCT}} \approx 19\,500\text{ cm}^{-1}$ observed in $\text{Ni}^{2+}:\text{ZnO}$ (Figure 6b), a value of $E_{\text{LMCT}} \approx 26\,300\text{ cm}^{-1}$ is thus predicted for $\text{Co}^{2+}:\text{ZnO}$. The reasonable agreement between this and the experimental (Figure 6a) transition energy for $\text{Co}^{2+}:\text{ZnO}$ supports assignment of the observed CT intensity at 25 200 cm^{-1} as a LMCT transition, although it does not preclude the presence of additional transitions in the same energy region.

Whereas the optical electronegativity model has been applied primarily to analysis of relatively localized donor and acceptor wave functions, the effective optical electronegativities active in the LMCT transitions of $\text{TM}^{2+}:\text{ZnO}$ may be strongly influenced by participation of the donor or acceptor in the semiconductor band structure. Strong perturbation of the acceptor TM^{2+} d orbitals can be ruled out by the applicability of

(30) Noras, J. M.; Allen, J. W. *J. Phys. C: Solid State Phys.* **1980**, *13*, 3511–3521.

(31) Heitz, R.; Hoffmann, A.; Broser, I. *Phys. Rev. B* **1993**, *48*, 8672–8682.

(32) Solomon, E. I.; Hanson, M. A. In *Inorganic Electronic Structure and Spectroscopy*; Solomon, E. I., Lever, A. B. P., Eds.; Wiley-Interscience: New York, 1999; Vol. II, pp 1–129.

(33) (a) Jørgensen, C. K. *Prog. Inorg. Chem.* **1970**, *12*, 101–158. $\chi_{\text{opt}}(\text{O}^{2-})$ values between 3.0 and 3.9 are reported, with 3.2 considered typical.

(34) Lever, A. B. P. *Inorganic Electronic Spectroscopy*, 2nd ed.; Elsevier Science Publishers: Amsterdam, The Netherlands, 1984, and references therein.

(35) Smith, G. P.; Liu, C. H.; Griffiths, T. R. *J. Am. Chem. Soc.* **1964**, *86*, 4796–4802.

the ligand-field model in interpreting the d–d transitions for both Co²⁺ and Ni²⁺ in ZnO and by the insensitivity of the ligand-field transition energies to quantum confinement effects. The oxide donor, however, is severely perturbed relative to a molecular oxyanion by its participation in the band structure of the semiconductor. Calculation of the effective optical electronegativity for the ZnO lattice oxide bound to Co²⁺ or Ni²⁺ using eqs 5 and 6 yields a value of only $\chi_{\text{opt}}(\text{O}^{2-}_{\text{ZnO}}) \approx 2.4$. This electronegativity is very low compared to that typical for O²⁻ ligands in molecular species ($\chi_{\text{opt}}(\text{O}^{2-}) \approx 3.2$).³³ The dopant-bound oxide is thus over 2 eV more easily oxidized than a typical molecular oxyanion. This perturbed electronegativity provides experimental evidence for the participation of the first coordination sphere of ligands around a TM²⁺ dopant in the extended band structure of ZnO, a factor that is extremely important in relation to the magnetic properties of this class of materials. Interestingly, the electronegativity of an oxygen atom directly bound to the dopant is greater than that of the lattice oxo in pure ZnO ($\chi_{\text{opt}}(\text{O}^{2-}_{\text{ZnO}}) \approx 2.0$),³⁶ suggesting partial electronic polarization by the dopant. Given these observations, it may be concluded that the oxo electronegativity, and hence the covalency of the TM²⁺-oxo bond, must be sensitive to the extent of quantum confinement in ZnO nanocrystals. From the magnitude of excitonic quantum confinement observed for ZnO nanocrystals and the known dependence of the valence band energy throughout this confinement regime,^{17,18} the total increase in $\chi_{\text{opt}}(\text{O}^{2-}_{\text{ZnO}})$ accessible experimentally is predicted to be only ca. 0.02 relative to bulk ZnO, and this sensitivity may be reduced further by local bond polarization effects as described above. The effect of quantum confinement on a dopant's electronic structure is therefore expected to be rather small, consistent with the lack of perturbation of the ligand-field fine structure energies (Section IV.D.i.).

In addition to energies, the intensities of the CT transitions are of fundamental importance because they reflect the covalency of the TM²⁺-ZnO bonding interactions and can be used to support the assignment of the observed charge-transfer transition in Co²⁺:ZnO. In the general case, the intensity of a CT transition is governed by covalent mixing of the donor and acceptor wave functions as described by eq 7a, where ψ_A and ψ_D are the unperturbed one-electron orbitals of the CT acceptor and donor, respectively.

$$\psi'_A = \sqrt{1 - c^2} (\psi_A) - c\psi_D \quad (7a)$$

$$c \approx \frac{-\langle \psi_A | H | \psi_D \rangle}{E_A - E_D} \quad (7b)$$

Theoretical and experimental studies³² indicate that the CT intensity is proportional to the square of the mixing coefficient, c , which in turn is proportional to the donor–acceptor resonance integral and inversely proportional to the mismatch in valence-shell ionization energies, E_A and E_D (eq 7b). The p–d (valence band – dopant) hybridization in II–VI semiconductors that gives rise to LMCT intensity is generally over an order of magnitude greater than the s–d (conduction band – dopant) hybridization that would give rise to MLCT intensity,^{37,38} and charge-transfer intensity should therefore be dominated by the

former. Intensity arguments thus provide further support for our assignment of the CT intensity at 25 200 cm⁻¹ in Co²⁺:ZnO as LMCT in character. In this regard, we note the presence of a broad and very weak negative MCD signal in Co²⁺:ZnO that extends throughout the visible energy range (Figure 6a). This MCD intensity displays $S = 3/2$ saturation behavior identical to that of the more pronounced Co²⁺ transitions and is therefore also attributable to the same chromophore. We hypothesize that this feature may be the Co²⁺-to-valence band (MLCT) transition, the intensity of which is an order of magnitude lower than that of the LMCT transition due to the very small orbital overlap between the donor (Co²⁺ d_e) and acceptor (conduction band) wave functions. Further experiments are planned to explore this possibility.

(iii) Zeeman Splittings and sp–d Exchange. The intense pseudo-A-term MCD feature at 28 000 cm⁻¹ in Figure 6a arises from the band gap transitions of ZnO. The $S = 3/2$ saturation magnetization behavior of this band gap MCD intensity indicates magnetization of the semiconductor due to interaction with the Co²⁺ dopants. This phenomenon, the so-called “giant Zeeman effect”,^{37,38} is of central importance to the potential spin-electronics applications of this DMS material. Experimentally, these 1.7% Co²⁺:ZnO DMS-QDs show an average band edge Zeeman shift of ca. 53 cm⁻¹/T over the range of 0–7 T (Figure 9b). Modeling these data quantitatively allows parametrization of the exchange coupling interactions responsible for this Zeeman effect.

The Zeeman data in Figure 9b are analyzed in the mean-field approximation using eq 8, where x is the dopant mole fraction and $\langle S_z \rangle$ is the expectation value of the S_z operator of the spin Hamiltonian. $N_0\alpha$ and $N_0\beta$ quantify the exchange interaction strengths between the dopant and unpaired spins in the conduction and valence bands, respectively.^{37–40}

$$\Delta E_{\text{Zeeman}}(\text{CB}) = xN_0\alpha\langle S_z \rangle \quad (8a)$$

$$\Delta E_{\text{Zeeman}}(\text{VB}) = xN_0\beta\langle S_z \rangle \quad (8b)$$

In the band gap excited state the conduction band electrons have majority Zn²⁺ character and the valence band electrons have majority oxo character. Consequently, $N_0\alpha$ and $N_0\beta$ are very different in magnitude.^{37,38,40} Whereas the exchange interaction between the dopant and a conduction band electron is Coulombic, the covalency of the oxo-Co²⁺ bond gives rise to strong direct antiferromagnetic exchange between the dopant and an unpaired valence band electron. The contribution from this p–d hybridization, $N_0\beta_{\text{hyb}}$, dominates the overall exchange magnitude and, therefore, $N_0\beta (\approx N_0\beta_{\text{hyb}}) \gg N_0\alpha$. In bulk Co²⁺-doped II–VI chalcogenide DMSs, for example, $N_0\beta$ typically exceeds $N_0\alpha$ by an order of magnitude.^{37,38,40} $N_0\alpha$ is also relatively independent of host lattice and was fixed at the typical value of +0.2 eV (+1600 cm⁻¹) for our analysis.^{37,38,40}

Figure 9a shows the ZnO band level Zeeman splitting pattern at the Γ point anticipated for H₁|z. At zero field, the 4-fold degeneracy of the cubic valence band (Γ_8) is removed in wurtzite ZnO with a splitting of ca. 56 cm⁻¹.⁴¹ Equation 8b now pertains

(37) Furdyna, J. K. *J. Appl. Phys.* **1988**, *64*, R29–R64.

(38) Kacman, P. *Semicond. Sci. Technol.* **2001**, *16*, R25–R39.

(39) Alawadhi, H.; Miotkowski, I.; Souw, V.; McElfresh, M.; Ramdas, A. K.; Miotkowska, S. *Phys. Rev. B: Condens. Matter* **2001**, *63*, 155201/1–10.

(40) Dietl, T.; Ohno, H.; Matsukura, F. *Phys. Rev. B: Condens. Matter* **2001**, *63*, 195205/1–21.

(36) (a) Duffy, J. A. *J. Phys. C: Solid State Phys.* **1980**, *13*, 2979–2989. (b) Duffy, J. A. *J. Chem. Phys.* **1977**, *67*, 2930–2931.

Table 2. Selected Values of $N_0\beta$ (eV) for Co^{2+} , Mn^{2+} , and Ni^{2+} -doped II–VI Semiconductors

	Co^{2+}	ref	Mn^{2+}	ref	Ni^{2+}
CdTe	−2.33	39	−0.83	40	
CdSe	−2.12	39	−1.30	40	
ZnTe	−3.03	39	−1.1	40	
ZnO	−2.3 (± 0.3) ^a		−2.7	40	−4.5(± 0.6) ^a

^a This work. Note: The values of $N_0\beta$ calculated here are for nanocrystals, and the other values presented are for bulk single crystals.

to the splitting of the $|\pm 3/2\rangle$ valence-band levels (Γ_9), and the $|\pm 1/2\rangle$ valence-band levels (Γ_7) split 1/3 as much. Within the approximations of this model, the experimental band edge Zeeman data for 1.7% Co^{2+} :ZnO DMS-QDs are best fit using a value of $N_0\beta = -2.3 \pm 0.3$ eV ($-18\,500 \pm 2400$ cm^{-1}) (Figure 9b), corresponding to an effective g value of $g_{\text{eff}} \approx 200$ for the Zeeman splitting of the Γ_9 valence band doublet. The energies shown in Figure 9a were calculated using the fitted results from Figure 9b. Implementation of a more sophisticated model for analysis of the Zeeman data is complicated by the anisotropies of the ZnO Zeeman splittings,^{42,43} optical selection rules,⁴³ and Co^{2+} magnetic susceptibility.⁴⁴ Preliminary modeling with inclusion of these anisotropies at fixed values estimated from the literature leads to a similar value of $N_0\beta$ but a poorer reproduction of the experimental data than that shown in Figure 9b. Expansion of the model to solve for the additional parameters is not warranted. Nevertheless, the data in Figure 9b clearly demonstrate a very large excitonic Zeeman effect in Co^{2+} :ZnO DMS-QDs and implicate large p–d exchange coupling. The mean field model described above allows an exchange magnitude of $N_0\beta \approx -2.3 \pm 0.3$ eV ($-18\,500$ cm^{-1}) to be estimated from the experimental Zeeman data.

Our experimental value of $N_0\beta$ is comparable to those measured or calculated for other II–VI DMSs (Table 2), but is somewhat smaller than that predicted for Co^{2+} :ZnO ($N_0\beta \approx -5$ eV (ca. $-40\,000$ cm^{-1})) by the method of scaling $N_0\beta$ with V^{-1} ($V =$ unit cell volume).^{5,45} This scaling method was applied to predict relative T_C values for ferromagnetism in ZnO DMSs in the absence of experimental values for $N_0\beta$, and our experimental value is therefore of interest for refining these predictions. Although phenomenologically valuable, the predictive approach of scaling $N_0\beta$ with V^{-1} does not account for differences in ligand electronegativities or for quantum confinement effects,⁴⁶ but only describes the dependence of $N_0\beta$ on changes in the metal–ligand orbital overlap. More quantitatively, $N_0\beta_{\text{hyb}}$ is described microscopically as arising from covalency of the Co^{2+} -oxide bonding interaction, parametrized in eq 9 in the context of a configuration interaction model.^{38,45,47}

$$N_0\beta_{\text{hyb}} \approx -\frac{1}{S} \left[\frac{\langle \psi_{\text{VB}} | \hat{H}_{\text{pd}} | \psi_{t_2} \rangle^2}{E_{\text{LMCT}}} \right] \quad (9)$$

The resonance integral in the numerator describes mixing between the Co^{2+} and the valence band and is proportional to

the metal–ligand orbital overlap. As noted previously,⁴⁵ this integral is relatively large in ZnO because of the small unit cell dimensions ($a = 3.2495$ Å, $c = 5.2067$ Å) and is expected to play a major role in determining the magnetic properties of ZnO DMSs as a group. The denominator, E_{LMCT} , describes the energetic mismatch between valence band and dopant acceptor wave functions and is defined experimentally for Co^{2+} :ZnO QDs by the assignment of the LMCT transition at $25\,200$ cm^{-1} in Figure 6a. This relatively high LMCT energy counteracts the reduced unit cell dimensions, and $N_0\beta$ is therefore not as large as predicted by the volumetric scaling factor alone.

It is noteworthy that the 5 K excitonic Zeeman effect and MCD observed in 1.5% Ni^{2+} :ZnO QDs is smaller than that observed in 1.7% Co^{2+} :ZnO QDs by at least an order of magnitude despite its substantially smaller LMCT energy (Figure 6). Assuming similar resonance integrals for Ni^{2+} and Co^{2+} (due to similar ionic radii), the magnitude of $N_0\beta$ in Ni^{2+} :ZnO is estimated to be ca. 1.9 times larger than that for Co^{2+} :ZnO using eq 9, the LMCT energies ($E_{\text{LMCT}} \approx 19\,500$ vs $25\,200$ cm^{-1}), and the spin states ($S = 1$ vs $3/2$) of these two ions. This enhanced $N_0\beta$ is not directly observed in the MCD or Zeeman data for Ni^{2+} :ZnO due to spin–orbit coupling within the Ni^{2+} ground state, discussed in the following section.

(iv) MCD Saturation Magnetization. MCD and SQUID magnetic susceptibility measurements of dilute frozen solutions of Co^{2+} :ZnO QDs show the $S = 3/2$ saturation behavior of the magnetically isolated Co^{2+} dopants (e.g., Figure 8a). The 4A_2 ground state of tetrahedral Co^{2+} has no orbital angular momentum and is consequently not split by in-state spin–orbit coupling or by the low-symmetry ligand field of wurtzite ZnO (Figure 8a). Out-of-state spin–orbit coupling, primarily with the nearby $^4T_1(\text{F})$ levels, gives rise to a small positive zero-field splitting of the ground state ($2D = +5.5$ cm^{-1}).^{20,48} This splitting causes the nesting observed in the saturation magnetization data for Co^{2+} :ZnO DMS-QDs shown in Figure 8a.

The MCD saturation magnetization data of Ni^{2+} :ZnO DMS-QDs show a substantially more complex behavior. The MCD data in Figure 8b deviate strongly from $S = 1$ spin-only behavior. Tetrahedral Ni^{2+} has a 3T_1 ground state that is subject to large first-order spin–orbit coupling and that is further influenced by the trigonal field of the wurtzite ZnO lattice. The ground-state multiplet splittings of Ni^{2+} in the wurtzite ZnO lattice are illustrated schematically in Figure 8b to the level of first-order spin–orbit coupling.^{19,49} Spin–orbit coupling within the tetrahedral $^3T_1(\text{F})$ term yields an A_1 ($J = 0$) ground state separated by 160 cm^{-1} and 260 cm^{-1} from the first and second excited levels, A_2 and E ($J = 1$), respectively. The energies of these levels have been estimated from magnetic susceptibility measurements on bulk single crystals of Ni^{2+} :ZnO and are accurate to within ca. ± 25 cm^{-1} .⁴⁹ The A_1 ground state is not degenerate and therefore does not split in a magnetic field, so $\langle S_z \rangle$ is nearly zero. The magnetic field does, however, induce mixing between the A_1 , A_2 , and E states (second-order Zeeman effect), and this gives rise to the observed temperature-dependent B-term MCD intensity, manifested most strikingly as the absence of saturation at high fields and low temperatures (Figure 8b). This second-order Zeeman effect is substantially weaker

(41) Thomas, D. G. *Phys. Chem. Solids* **1960**, *15*, 86–96.

(42) Gubarev, S. I. *Phys. Status Solidi B* **1986**, *134*, 211–222.

(43) Arciszewska, M.; Nawrocki, M. *J. Phys. Chem. Solids* **1986**, *47*, 309–314.

(44) Brumage, W. H.; Dorman, C. F.; Quade, C. R. *Phys. Rev. B: Condens. Matter* **2001**, *63*, 104411/1–4.

(45) Blinowski, J.; Kacmar, P.; Dietl, T. *cond-mat/0201012*.

(46) Kyrchenko, F. V.; Kossut, J. *cond-mat/0112220*.

(47) Bhattacharjee, A. K. *Phys. Rev. B* **1992**, *46*, 5266–5273.

(48) Mao-Lu, D.; Min-Guang, Z. *J. Phys. C: Solid State Phys.* **1988**, *21*, 1561–1569.

(49) Brumage, W. N.; Lin, C. C. *Phys. Rev.* **1964**, *134*, 950–957.

than the first-order Zeeman splitting active in the ⁴A₂ ground state of Co²⁺ in ZnO, and consequently $\Delta E_{\text{Zeeman}}(\text{VB})$ in eq 8 is nearly an order of magnitude smaller for Ni²⁺:ZnO than for Co²⁺:ZnO, despite the greater magnitude of $N_0\beta$ in the former determined above.

(v) Ferromagnetism in Co²⁺:ZnO DMS-QD Aggregates.

Theory predicts that doping ZnO and other II–VI semiconductors with first-row TM²⁺ ions should yield ferromagnetically ordered phases.^{4,5} The free-standing Co²⁺:ZnO DMS-QDs show no evidence of long-range magnetic ordering, however, but instead show the saturation magnetization behavior of the isolated paramagnetic dopants (e.g., Figure 8). This picture changes dramatically when the DMS-QDs are allowed to aggregate under reaction-limited conditions.⁵⁰ The inset to Figure 10b shows an SEM image of the micron-scale structures formed upon slow aggregation of 4.9 nm diameter 3.6% Co²⁺:ZnO DMS-QDs from ethanol at room temperature. TEM images of related Ni²⁺:ZnO aggregates (to be published elsewhere⁵⁰) show dense but disordered structures with clear retention of the individual nanocrystal shapes and sizes. Powder X-ray diffraction measurements of the aggregated and nonaggregated samples show identical diffraction patterns and verify the absence of new phases in the aggregated samples. Room-temperature magnetic susceptibility measurements of these aggregates show rapid magnetic saturation at low fields and a clear magnetic hysteresis (Figure 10a), indicative of ferromagnetism. This ferromagnetism persists well above room temperature, with $T_C > 350$ K (Figure 10b).

An estimate of the ferromagnetic saturation moment per cobalt may be made by using the low-temperature $S = 3/2$ saturation magnetization as an internal reference. At room temperature, the magnetization is dominated by the ferromagnetic component, but at low temperatures both ferromagnetic and paramagnetic signals can be observed, indicating the presence of substantial magnetically isolated Co²⁺. For the 3.6% Co²⁺:ZnO DMS-QD aggregates shown in Figure 10, ca. 10% of all 10 K magnetization comes from ferromagnetism, from which we estimate a 300 K ferromagnetic saturation moment of ca. 0.3 μ_B /cobalt (10% of 3 μ_B /cobalt). This value is likely an overestimate, however, because of the effects of antiferromagnetism and spin-glass behavior which may render some dopants magnetically silent. We emphasize that this remarkable transformation of magnetic properties from paramagnetic to ferromagnetic occurs in the absence of any elevated-temperature annealing or other post-aggregation treatment and simply results from the formation of bonds between otherwise stable paramagnetic nanocrystals. The ferromagnetism we observe in Co²⁺:ZnO is therefore unambiguously associated with the substitutional dopants characterized in the previous sections of this paper and does not arise from phase segregation effects.

We attribute the appearance of ferromagnetism upon aggregation to two factors: (i) introduction of interface defects, which introduces an interdopant coupling mechanism and (ii) the greater domain sizes of the aggregates than of the colloidal nanocrystals. The latter results in greater magnetocrystalline anisotropy energies (MAEs) and is critical to the observation of a hysteresis. The MAE, given by the product of the magnetocrystalline anisotropy factor, K , and the domain volume, V , determines the barrier height to magnetization reversal in a

single-domain magnetic material.⁵¹ The lifetime of the magnetization is related to the barrier height as described by eq 10 (where τ_0 is the inverse attempt frequency, related to the Larmor precession frequency, and is on the order of 10⁻⁹ s).

$$\tau = \tau_0 \exp[KV/kT] \quad (10)$$

If the MAE is small relative to the available thermal energy, as in nanocrystals of very small volumes, magnetic equilibration occurs rapidly and magnetic hysteresis is not observed. Evidence for increased domain sizes comes from analysis of the curvature of the 300 K saturation magnetization data (Figure 10a) using the Brillouin function to determine a lower limit for the effective spin state of the ferromagnetic domains. The rapid 300 K saturation in Figure 10a implicates an effective spin state of at least $S \approx 8000$, which would require domains comprising at least ca. 5000 Co²⁺ ions. At 3.6% Co²⁺ doping of 4.9 nm diameter QDs, the average nanocrystal will contain ca. 200 Co²⁺ ions, and the minimum effective aggregate size required to form a single ferromagnetic domain is therefore ca. 25 nanocrystals. At these sizes, domain wall formation may be anticipated. Although this lower limit is likely well below the actual domain size, it illustrates that the effective domain is far greater than a single nanocrystal. In addition to increasing domain sizes, however, aggregation likely also introduces an essential mechanistic component required for ferromagnetic ordering, since the free-standing nanocrystals show only paramagnetism and not superparamagnetism. We hypothesize that this critical component relates to defects at the nanocrystal fusion interfaces formed during aggregation. Such defects, responsible for making ZnO naturally n -type in many instances, could provide the necessary source of carriers required to mediate ferromagnetic ordering among dopants via the proposed double-exchange, RKKY, or Zener mechanisms.^{4,5} Experiments to test this hypothesis are currently in progress.

V. Conclusion

We have developed a new and facile procedure for the synthesis of colloidal ZnO and transition-metal-doped ZnO nanocrystals. This procedure, involving hydrolysis and condensation in DMSO at room temperature, provides high-quality ZnO quantum dots with reasonable shape and size distributions. Transition-metal doping was accomplished by introducing transition-metal cations into the initial Zn²⁺ starting solutions, and the specific cases of Co²⁺ and Ni²⁺ doping have been explored in detail. The results of our mechanistic studies demonstrate that the coordination chemistry of the dopant ion strongly influences both the nucleation and growth of ZnO nanocrystals, even at low dopant concentrations and in cases of excellent dopant/host compatibility (e.g., Co²⁺ in ZnO). This synthetic procedure allows the relatively rapid preparation of gram quantities of doped quantum dots in open containers with no need for special precursors, precautions to avoid atmospheric contamination, or temperature stabilization. Subsequent ligand exchange processing provides extremely dispersible TOPO-treated ZnO DMS-QDs, and this treatment was demonstrated to also be very effective in removing dopant ions from the nanocrystal surfaces, thereby ensuring exclusively internal doping in the final colloids.

(50) Radovanovic, P. V.; Gamelin, D. R. *Phys. Rev. Lett.*, in press.

(51) Majetich, S. A.; Scott, J. H.; Kirkpatrick, E. M.; Chowdary, K.; Gallagher, K.; McHenry, M. E. *Nanostruct. Mater.* **1997**, *9*, 291–300.

Our preparation of ZnO DMS-QDs was motivated by the current interest in magnetic semiconductors that display giant Zeeman splittings and high- T_C ferromagnetism for magneto-optic and magneto-electronic applications. Using low-temperature MCD and Zeeman spectroscopies, we have studied the spin-exchange interaction between dopants and the ZnO QD host in $\text{Co}^{2+}:\text{ZnO}$ DMS-QDs and have determined the magnitude of the p-d exchange coupling constant, $N_0\beta \approx -2.3 \pm 0.3$ eV ($-18\,500\text{ cm}^{-1}$). Analysis of the sub-bandgap LMCT transitions in both $\text{Co}^{2+}:\text{ZnO}$ and $\text{Ni}^{2+}:\text{ZnO}$ DMS-QDs has allowed $N_0\beta \approx -4.5 \pm 0.6$ eV ($-36\,300\text{ cm}^{-1}$) to be calculated for the latter material. The smaller Zeeman effect in $\text{Ni}^{2+}:\text{ZnO}$ than in $\text{Co}^{2+}:\text{ZnO}$ has been related to the spin-orbit splitting of the Ni^{2+} ground state. Finally, we have observed room-temperature ferromagnetism in nanostructured aggregates of $\text{Co}^{2+}:\text{ZnO}$ DMS-QDs prepared from these paramagnetic colloids at room temperature. This observation unambiguously verifies the existence of intrinsic high- T_C ferromagnetism in $\text{Co}^{2+}:\text{ZnO}$ and validates our chemical approach to the synthesis and study of magnetic semiconductor materials. Future experiments will explore the use of colloidal DMS-QDs as highly processable building-block precursors for the construction of more sophisticated ferromagnetic semiconductor architectures for potential spintronics applications.

Acknowledgment. Financial support from the National Science Foundation (DMR-0239325 and ECS-0224138) is gratefully acknowledged. Acknowledgment is also made to the Research Corporation (RI0832), the ACS-PRF (37502-G), the

Semiconductor Research Corporation (2002-RJ-1051G), and the University of Washington (RRF-2651) for partial support of this research. N.S.N. thanks the UW/PNNL Joint Institute for Nanoscience for a graduate fellowship. TEM data were collected at the EMSL, a national scientific user facility sponsored by DOE's Office of Biological and Environmental Research, located at Pacific Northwest National Laboratory, operated for DOE by Battelle. The authors thank Dr. Chongmin Wang (PNNL) for valuable assistance with the TEM measurements.

Supporting Information Available: Six figures: (S1) Kinetics data showing band gap energies and intensities measured as a function of time after addition of $\text{N}(\text{Me})_4\text{OH}$ to a DMSO solution of $\text{Zn}(\text{OAc})_2$ containing Ni^{2+} or Co^{2+} . (S2) Absorption spectra recorded during the TOPO treatment of ZnO QDs with cobalt intentionally bound to the surface. (S3) TEM and electron diffraction data for TOPO-treated Ni^{2+} -doped ZnO nanocrystals. (S4) 300 K luminescence data for pure ZnO QDs and 2.0% $\text{Co}^{2+}:\text{ZnO}$ DMS-QDs in EtOH. (S5) Comparison of room-temperature $\text{Co}^{2+}:\text{ZnO}$ LF absorption spectra of the bulk single crystal, the DMS-QDs described here, and the DMS-QDs prepared by the ICS procedure (ref 13). (S6) Comparison of the room-temperature ZnO band gap absorption spectra of 4.2 nm ZnO quantum dots before and after TOPO treatment (PDF). This material is available free of charge via the Internet at <http://pubs.acs.org>.

JA036811V